Supporting Information

High-dimensional in-sensor reservoir computing with optoelectronic memristors for high-performance neuromorphic machine vision

Yoon Ho Jang,† Joon-Kyu Han,† Sangik Moon, Sung Keun Shim, Janguk Han, Sunwoo Cheong, Soo Hyung Lee, and Cheol Seong Hwang*

†These authors equally contributed to this work.
*E-mail: cheolsh@snu.ac.kr

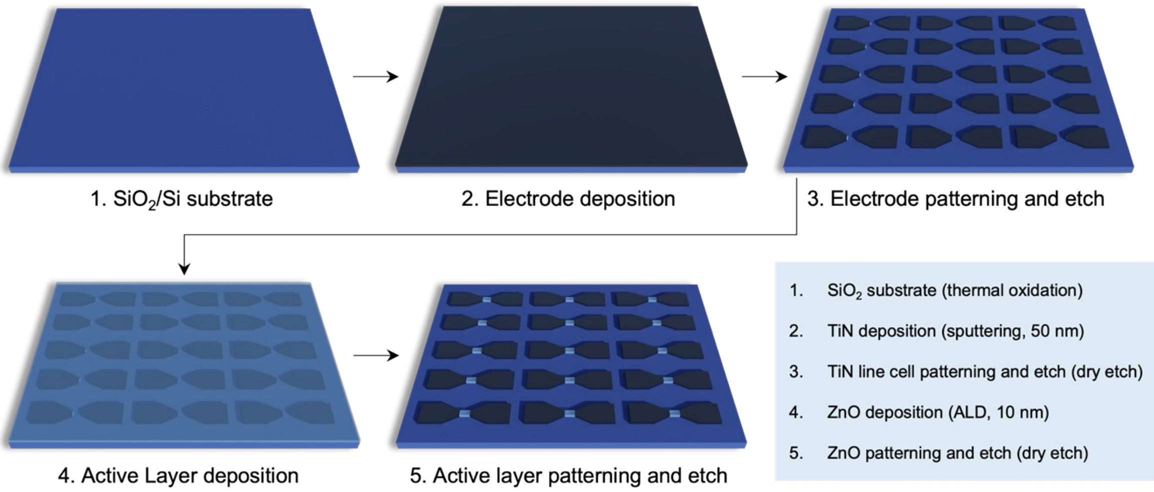

Fig. S1 Fabrication of the ZnO optoelectronic memristors. Schematic illustration of procedures to fabricate the ZnO optoelectronic memristors.

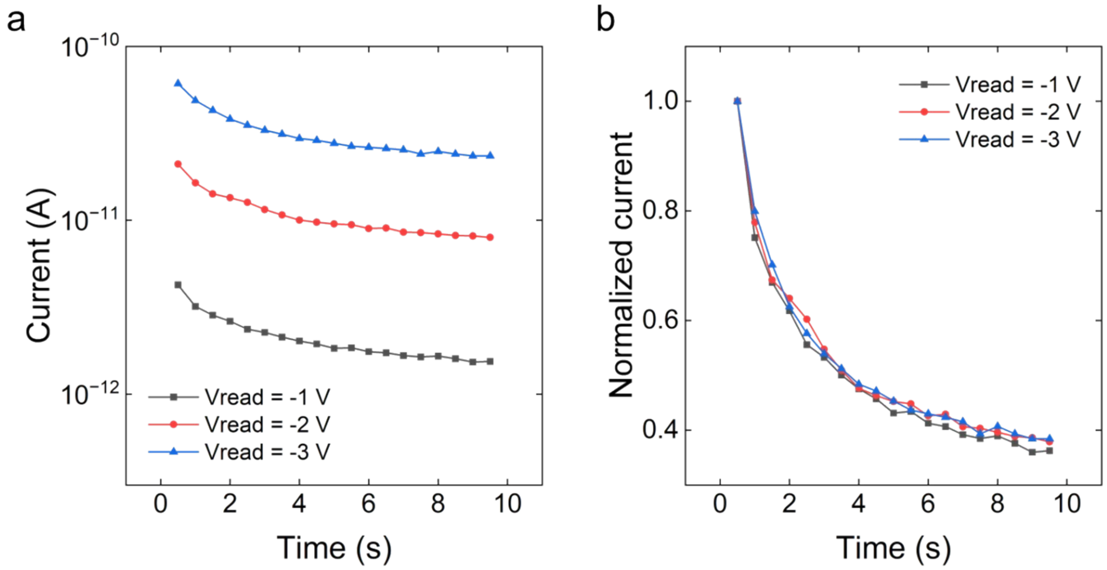

Fig. S2 Conductance relaxation of ZnO memristor according to read voltage. (a) Conductance evolution of ZnO memristor with read voltages of -1, -2, and -3 V. The memristor conductance was read with 0.5-second intervals following a 5-second exposure to white light. (b) Normalized current for the conductance evolution with read voltages of -1, -2, and -3 V.

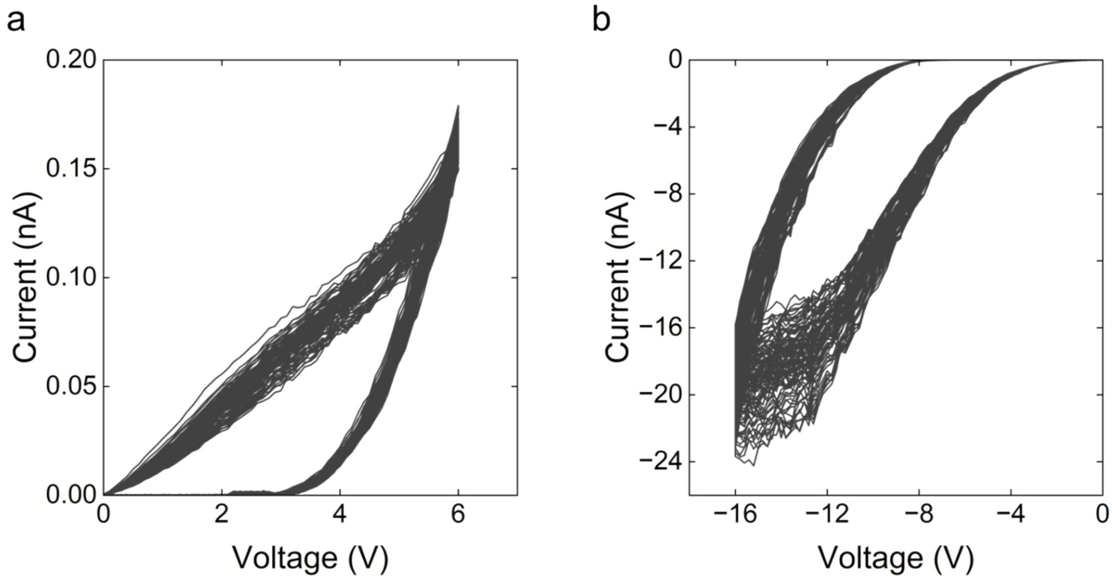

Fig. S3 I-V plot with a linear scale for the positive (a) and negative (b) sweep in the 100 DC cycle of **Fig.1a**.

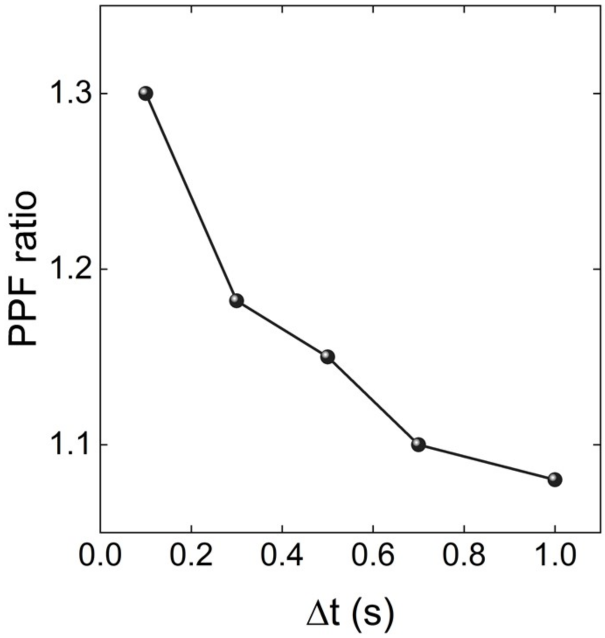

Fig. S4 A pair-pulse facilitation (PPF) function, where the PPF ratio decreased when the time interval increased.

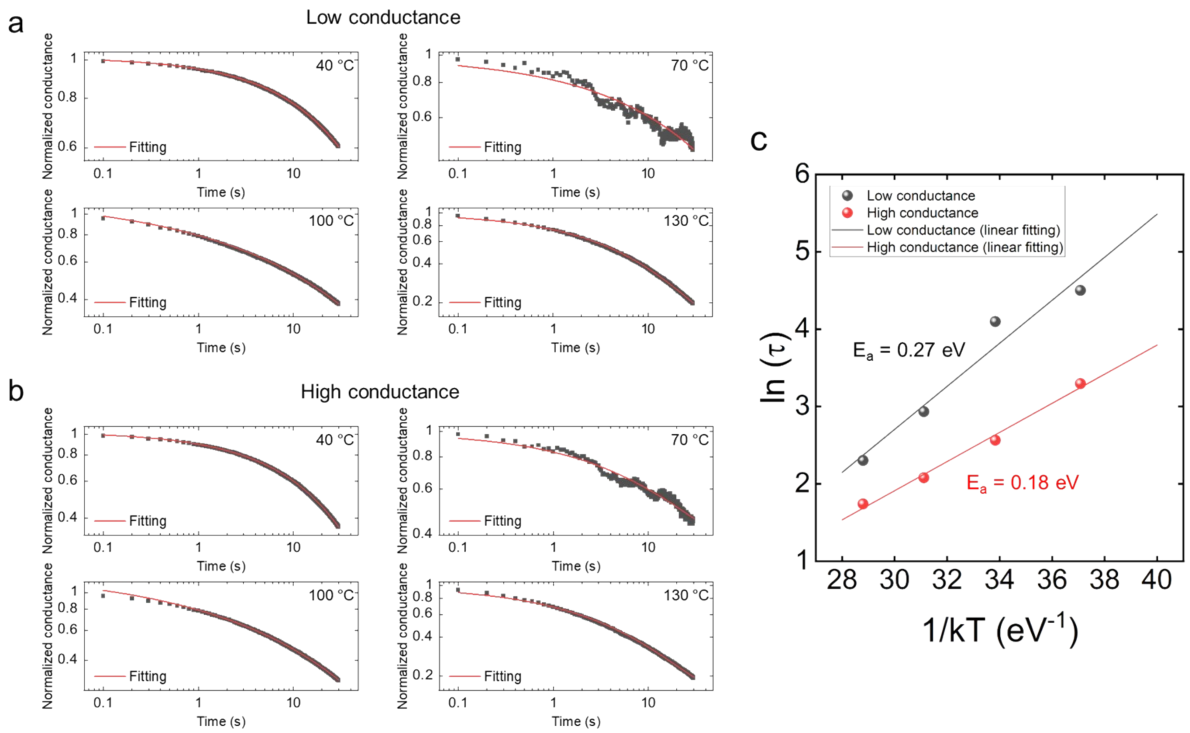

Fig. S5 The trap depth of the ZnO, determined by analyzing the time-dependent current-relaxation characteristics of the low and high conductance states at different temperatures. (a) The relaxation curves of the low conductance state at various temperatures. (b) The relaxation curves of the high conductance state at different temperatures. The current decreased as the trapped electrons in the active layer were released (detrapped). During this test, the current was measured at a reading voltage of -3 V for 30 seconds, while the temperature was varied between 40 °C and 130 °C. The read current was normalized to the initial current at $t = 0$ and fitted into the stretched exponential function [$f_\beta(t) = Ae^{-\left(\frac{t}{\tau}\right)^\beta} + B$] to extract the time constant (τ) at each temperature. (c) The Arrhenius plots of ln(τ) versus 1/kT of the low and high conductance states. The activation energy of the low conductance state was 0.27 eV, while that of the high conductance state was 0.18 eV.

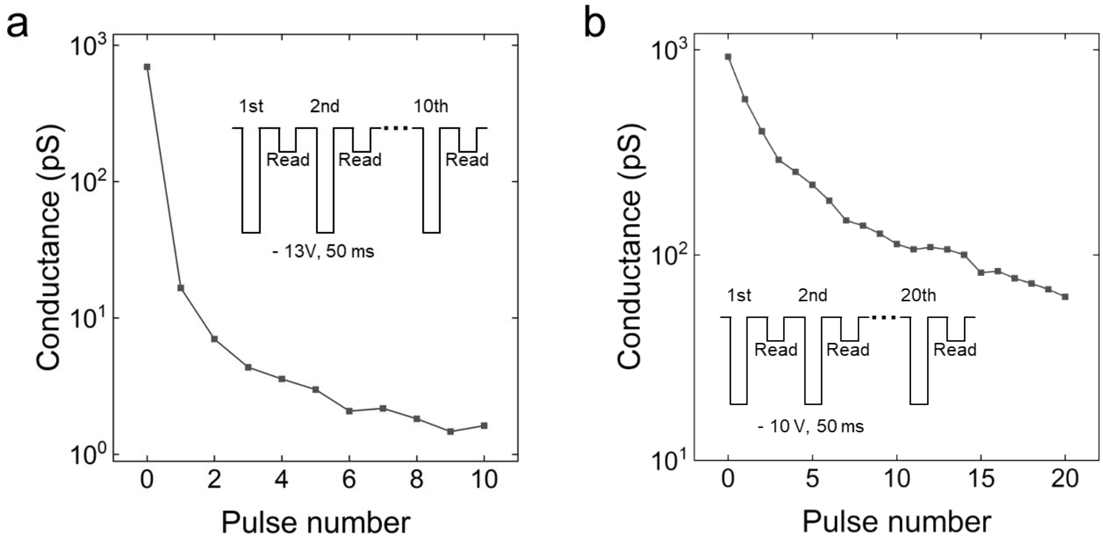

Fig. S6 The conductance as a function of the number of electrical pulses, demonstrating the operation of the electrical mask. (a) Conductance modulation with – 13V pulse. (b) Conductance modulation with – 10 V pulse.

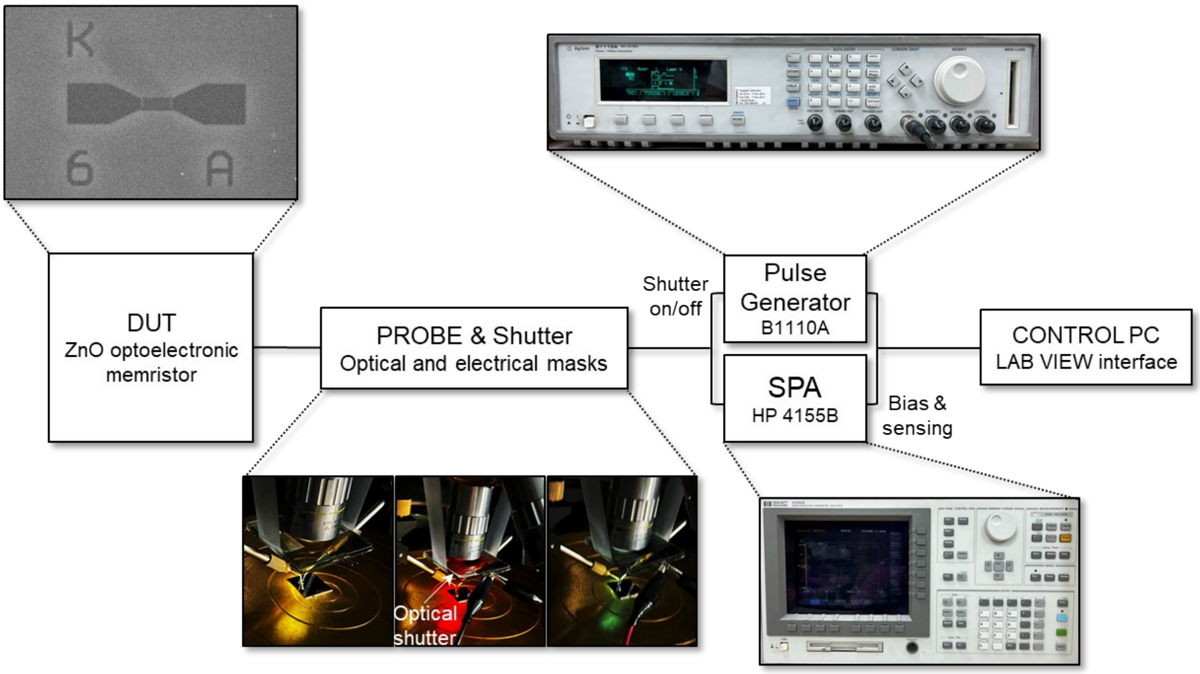

Fig. S7 Measurement flow for the in-sensor reservoir operations. The measurement setup consists of an optical shutter that controls the application of optical pulses, a pulse generator (PG) that provides the electrical pulse stream to the optical shutter, and a semiconductor parameter analyzer (SPA) that measures the conductance of the optoelectronic memristors.

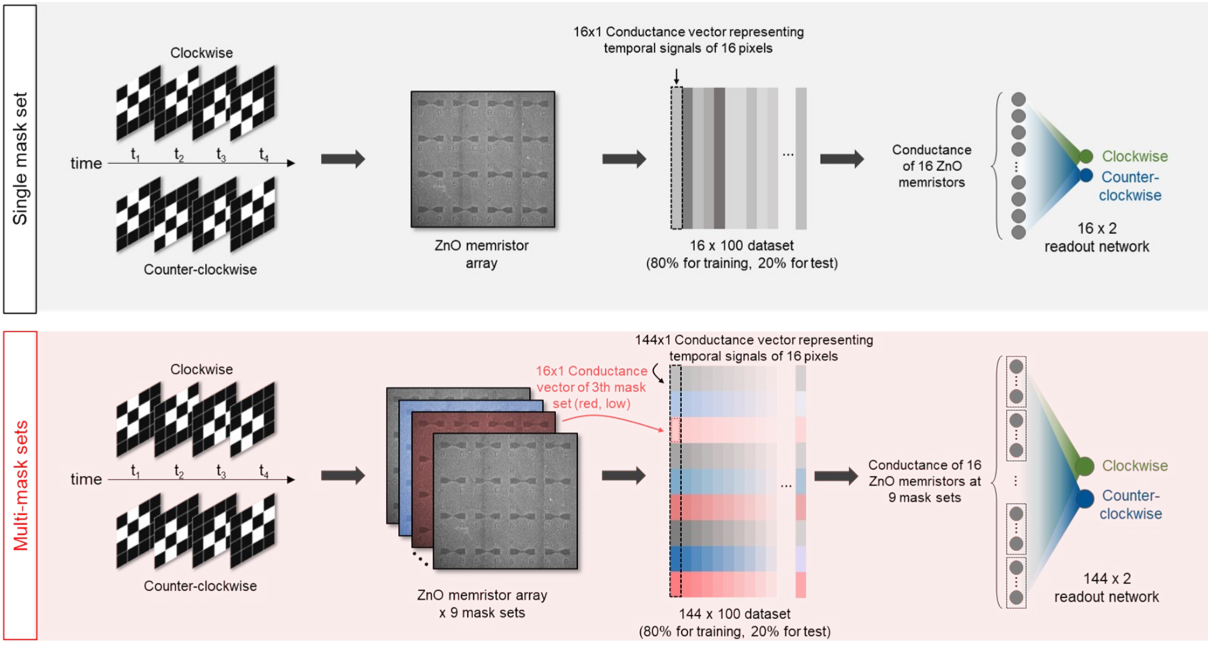

Fig. S8 Schematic illustration of the process of clockwise and counter-clockwise motion perception.

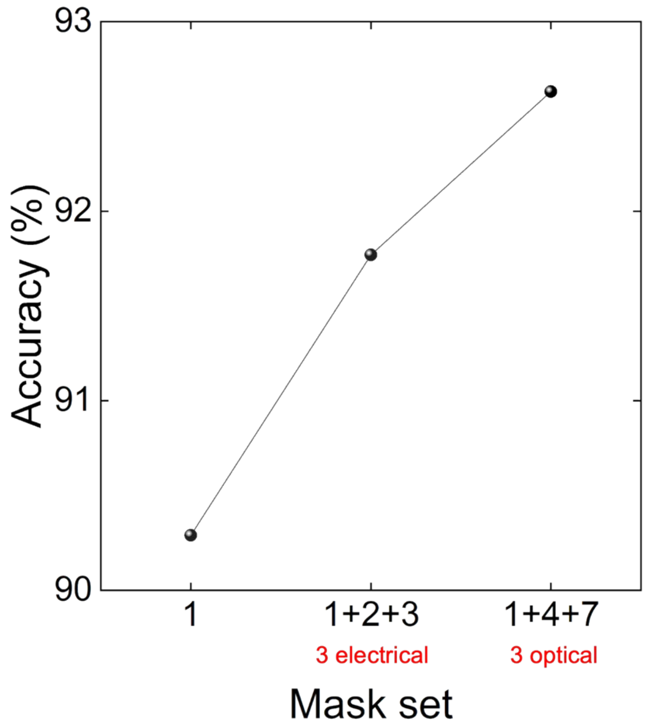

Fig. S9 Classification accuracies of three cases, when only mask set 1 was used (baseline), when mask sets 1, 2, and 3 were used, and when mask sets 1, 4, and 7 were used.

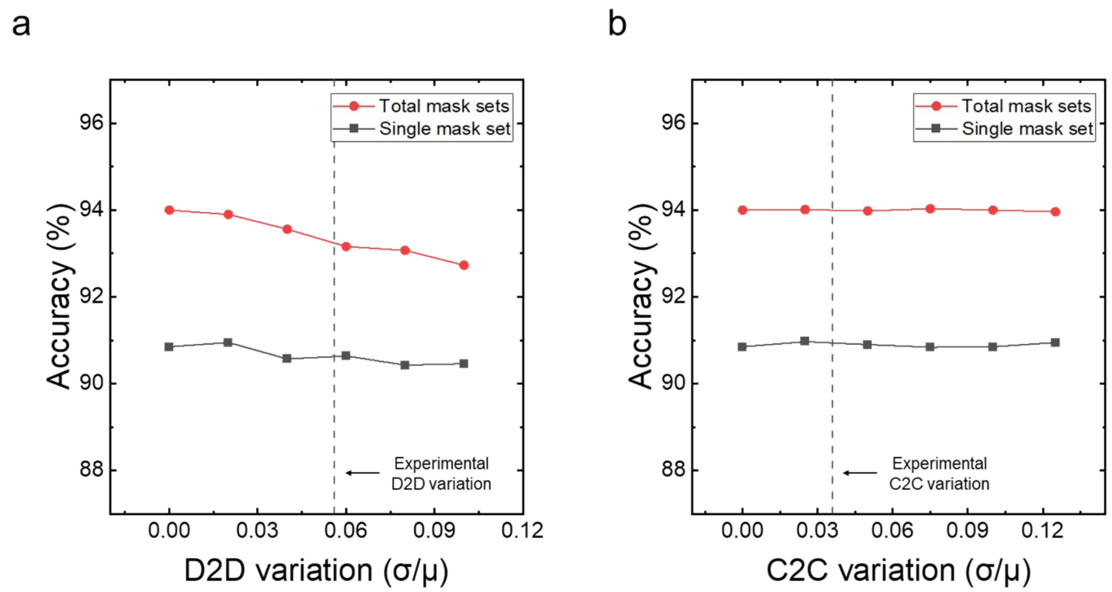

Fig. S10 MNIST recognition results when D2D (a) and C2C (b) variations are incorporated. The variations were derived from the cycling and device uniformity test outcomes in Figures 2c and d. A red, low mask set was utilized for the single mask set.

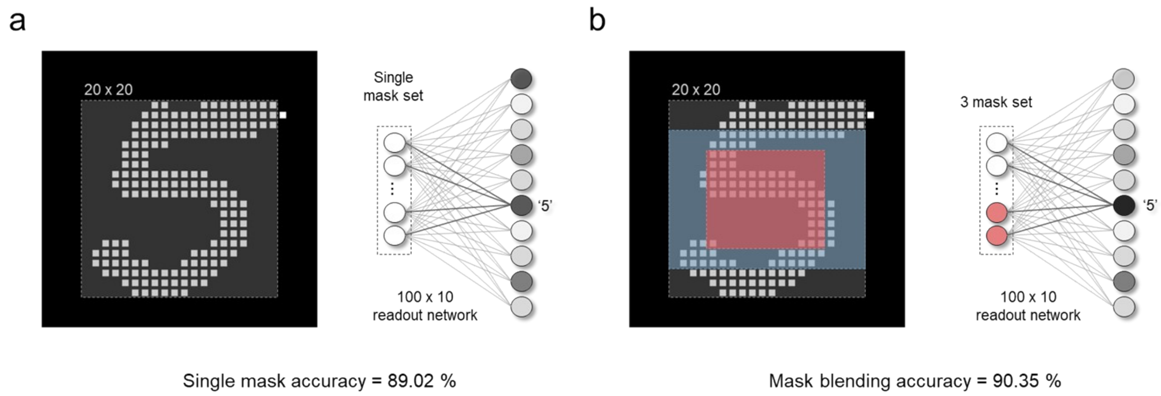

Fig. S11 Mask blending technique. (a) Recognition test results for the 20×20 MNIST data utilizing a single mask set (red and low) (b) Mask blending results for the 20×20 MNIST data utilizing 3 mask sets (white and low; blue and low; red and low)

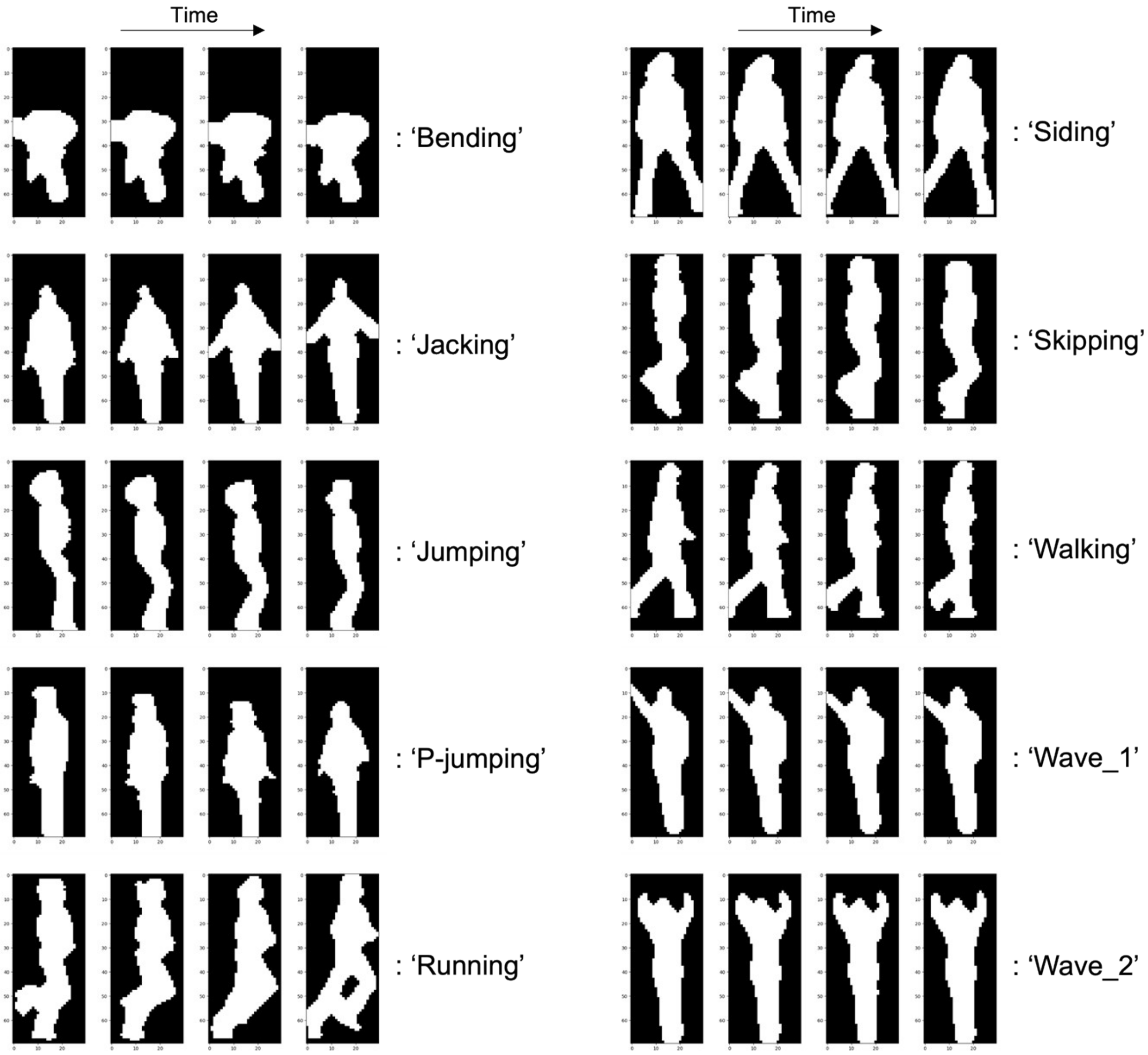

Fig. S12 Pre-processed images for the 10 types of human action. Original images were binarized and chopped into 70×30.

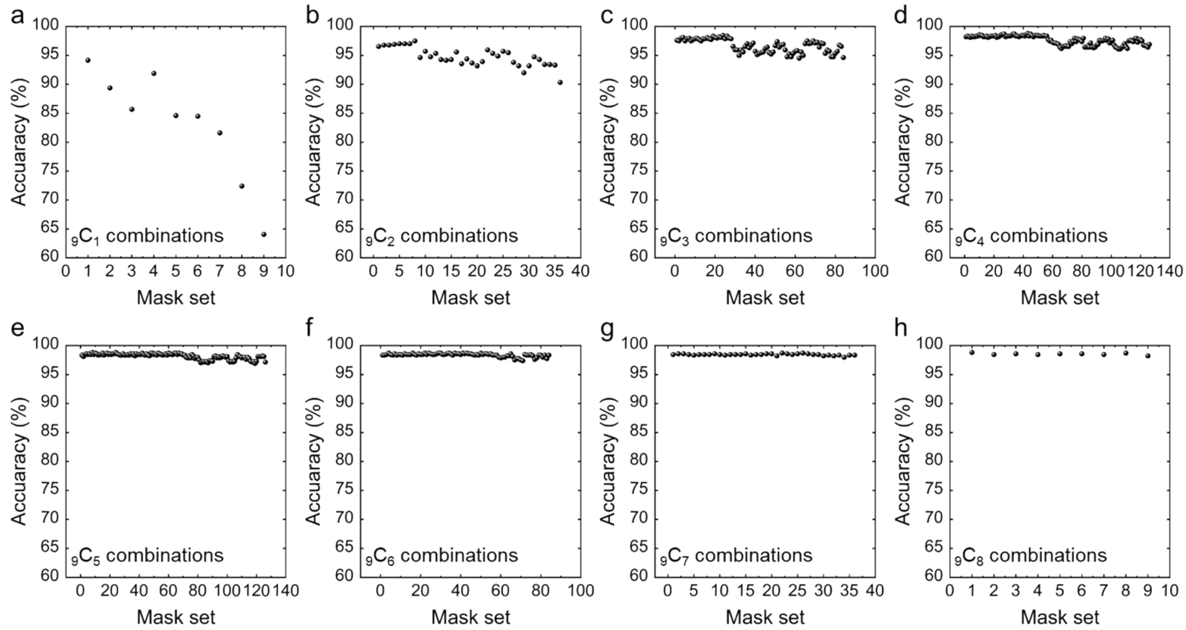

Fig. S13 The recognition accuracy of human action pattern recognition for all mask set combinations (a) 9 combinations of one mask set, (b) 36 combinations of two mask sets, (c) 84 combinations of three mask sets, (d) 126 combinations of four mask sets, (e) 126 combinations of five mask sets, (f) 84 combinations of six mask sets, (g) 36 combinations of seven mask sets, and (h) 9 combinations of eight mask sets. Higher recognition accuracy was achieved when the number of mask sets increased.

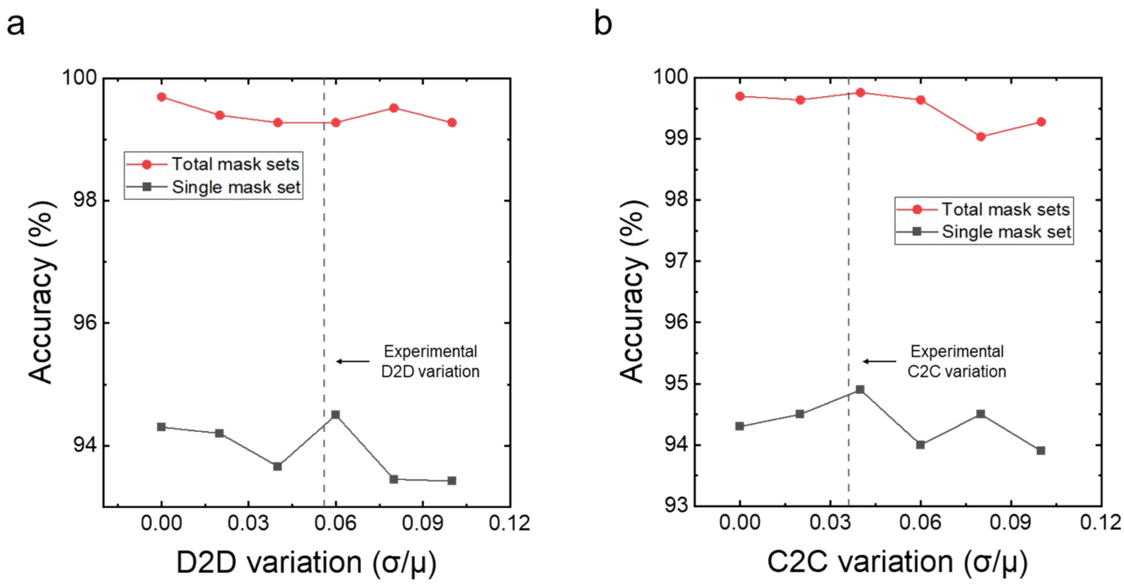

Fig. S14 Human action recognition results when D2D (a) and C2C (b) variations are incorporated. The variations were derived from the cycling and device uniformity test outcomes in Figures 2c and d. A white, low mask set was utilized for the single mask set.

Table S1 The initial conductance for 3 electrical and 3 optical masks.

	White	Blue	Red
Low	0.3 pS	0.3 pS	0.3 pS
Middle	3 pS	3 pS	3 pS
High	33 pS	33 pS	8 pS

Table S2 Comparison table of previously reported optoelectronic devices for in-sensor RC

Ref	**Active layer**	**Light**	**Application**	**Bit**	**Maximum power consumption**	**Dimensionality enhancement**	**MNIST accuracy**
S1	SnS	Visible light	Language learning	5	~30 nW	-	-
S2	MoS_2	Visible light	4-digit numbers recognition	4	~300 nW	-	-
S3	α-In_2Se_3	Red	MNIST & QR code recognition	4	~75 pW	Through additional terminal (back-gate)	86.1 %
S4	GaO_x	Ultra-violet	Fingerprint recognition	4	20 nW	-	-
S5	ZnO:N/ IGZO	Ultra-violet	MNIST & humanaction recognition	4	~0.6 nW	-	90.45 %
S6	MoS_2	Red	Action recognition	4	~800 nW	-	-
This work	**ZnO**	**White light**	**MNIST & human action recognition**	**4**	**1.2 nW**	**Through optical & electrical masks**	**94.1 %**

References

S1 L. Sun, Z. Wang, J. Jiang, Y. Kim, B. Joo, S. Zheng, S. Lee, W. J. Yu, B.-S. Kong and H. Yang, *Sci. Adv.*, 2021, **7**.

S2 W. Du, C. Li, Y. Huang, J. Zou, L. Luo, C. Teng, H.-C. Kuo, J. Wu and Z. Wang, *IEEE Electron Device Lett.*, 2022, **43**, 406–409.

S3 K. Liu, T. Zhang, B. Dang, L. Bao, L. Xu, C. Cheng, Z. Yang, R. Huang and Y. Yang, *Nat Electron*, 2022, **5**, 761–773.

S4 Zhang, X. Zhao, X. Zhang, X. Hou, X. Ma, S. Tang, Y. Zhang, G. Xu, Q. Liu and S. Long, *Nat Commun*, 2022, **13**.

S5 Y. Sun, Q. Li, X. Zhu, C. Liao, Y. Wang, Z. Li, S. Liu, H. Xu and W. Wang, *Advanced Intelligent Systems*, 2022, **5**.

S6 J. Chen, Z. Zhou, B. J. Kim, Y. Zhou, Z. Wang, T. Wan, J. Yan, J. Kang, J.-H. Ahn and Y. Chai, *Nat. Nanotechnol.*, 2023, **18**, 882–888.